NANO · MICRO small
www.small-journal.com

Mesoscopic 3D Charge Transport in Solution-Processed Graphene-Based Thin Films: A Multiscale Analysis

Alex Boschi, Alessandro Kovtun, Fabiola Liscio, Zhenyuan Xia, Kyung Ho Kim, Samuel Lara Avila, Sara De Simone, Valentina Mussi, Carlo Barone, Sergio Pagano, Marco Gobbi, Paolo Samorì, Marco Affronte, Andrea Candini, Vincenzo Palermo, and Andrea Liscio**

Graphene and related 2D material (GRM) thin films consist of 3D assembly of billions of 2D nanosheets randomly distributed and interacting via van der Waals forces. Their complexity and the multiscale nature yield a wide variety of electrical characteristics ranging from doped semiconductor to glassy metals depending on the crystalline quality of the nanosheets, their specific structural organization ant the operating temperature. Here, the charge transport (CT) mechanisms are studied that are occurring in GRM thin films near the metal-insulator transition (MIT) highlighting the role of defect density and local arrangement of the nanosheets. Two prototypical nanosheet types are compared, i.e., 2D reduced graphene oxide and few-layer-thick electrochemically exfoliated graphene flakes, forming thin films with comparable composition, morphology and room temperature conductivity, but different defect density and crystallinity. By investigating their structure, morphology, and the dependence of their electrical conductivity on temperature, noise and magnetic-field, a general model is developed describing the multiscale nature of CT in GRM thin films in terms of hopping among mesoscopic bricks, i.e., grains. The results suggest a general approach to describe disordered van der Waals thin films.

1. Introduction

Graphene and related 2D material (GRMs) can be manufactured with a variety of protocols yielding samples composed of sheets with different sizes, compositions and properties. These methods are also characterized by different cost, scalability and yield. Among them, liquid-phase exfoliation methods can be successfully employed to generate large volumes of highly concentrated inks by dispersing bulk multi-layered crystals in a given solvent and providing energy to the system to overcome the weak van der Waals (vdW) interactions keeping adjacent sheets together. Sheets obtained by exfoliation comprise typically a mixture of mono- and multi-layer thickness,[1] and display defects with different dimensionality,[2] including (0D) dopants and topological defects, (1D) grain boundaries, edges and in-plane heterojunctions, and (2D) wrinkling, folding, and scrolling, whose

A. Boschi, A. Kovtun, Z. Xia, A. Candini, V. Palermo
Consiglio Nazionale delle Ricerche
Istituto per la Sintesi Organica e la Fotoreattività
(CNR-ISOF), via Gobetti 101, Bologna 40129, Italy
E-mail: vincenzo.palermo@isof.cnr.it

A. Boschi
Istituto Italiano di Tecnologia
IIT – CNI
Laboratorio NEST
piazza S. Silvestro 12, Pisa 56127, Italy

The ORCID identification number(s) for the author(s) of this article can be found under https://doi.org/10.1002/smll.202303238

DOI: 10.1002/smll.202303238

F. Liscio
Consiglio Nazionale delle Ricerche
Istituto per la Microelettronica e Microsistemi
(CNR-IMM) – Bologna Unit
via Gobetti 101, Bologna 40129, Italy

Z. Xia
Chalmers University of Technology
Department of Industrial and Materials Science
Kemivägen 9, Gothenburg 41296, Sweden

K. H. Kim, S. L. Avila
Chalmers University of Technology
Department of Microtechnology and Nanoscience
Kemivägen 9, Gothenburg 41296, Sweden

K. H. Kim
Physics Department
Royal Holloway
University of London
Egham, Surrey TW20 0EX, UK

S. De Simone, V. Mussi, A. Liscio
Consiglio Nazionale delle Ricerche
Istituto per la Microelettronica e Microsistemi
(CNR-IMM) – Roma Unit
via del Fosso del Cavaliere 100, Roma 00133, Italy
E-mail: andrea.liscio@artov.imm.cnr.it

number depend on the production method used and on the experimental conditions. Such defects are not only suitable reactive sites for chemical functionalization but are also bottlenecks for charge transport as they act as traps or scattering centers for charges. Hence, they represent an additional degree of complexity when modeling charge transport mechanisms (CT) in 2D materials. Nevertheless, the control of CT properties (i.e., mobility, conductivity, etc.) is crucial for technological applications in large-area electronics.[3] GRM suspensions can be processed into thin films consisting of 3D assembly of billions of 2D nanosheets mostly aligned in-plane and interacting via vdW forces (a.k.a. 2D van der Waals thin film).[3a] When describing thin films, in addition to the defects existing in single nanosheets, one has to take into account the disorder in their packing during the deposition which can form domains with different degrees of order and 2D/3D aggregates at mesoscale and empty spaces. For example, the presence of 2D defects in the first nanosheets deposited on a substrate induces further disorder in the arrangement of the upper nanosheets which produces long-range distortion (cumulative disorder).[4]

CT through such films is therefore a multi-scale and multi-dimensional process comprising two contributions to the charge-carrier propagation at the nanometric scale: intrinsic or intra-sheet, i.e., within the individual flake, and extrinsic or inter-sheet, i.e., between neighboring nanosheets. Upon increasing the length-scale the description of the interplay of such two contributions becomes extremely complicated due to the enormous number of unevenly arranged sheets. In essence, we can distinguish three length scales involving different structures, defects and processes:

1) *nanoscale*: tessellation defects of single nanosheet, sheet-sheet local stacking;
2) *mesoscale*: domains and inter-domain boundaries;
3) *macroscale*: thin film as composite polycrystalline bulk material.

Therefore, the macroscale CT results as the contribution of all the intrinsic and extrinsic charge-carrier propagation processes, both inside the domain and at their boundaries.

The role of structural disorder and dimensionality has been shown in some recent works. Kelly et al.[5] investigated the role of film porosity (i.e., nanosheet alignment and network connectivity) and showed that CT is heavily influenced by the deposition method, the post-treatment regime, the nanosheet properties and the inter-sheet junctions. Moreover, by investigating printed thin films based on different 2D nanosheets (few-layer graphene, molybdenum disulfide, and titanium carbide MXene) Piatti et al.[5] clearly showed the strong dependence of the dimensionality of CT.

In this article, we consider the simultaneous role of the defects and the structural disorder in order to develop a multiscale description of CT that takes into account the local structure of 2D van der Waals thin films. In particular, we develop a general framework to describe CT in GRM thin films as in semicrystalline conjugated polymers. We show that GRM thin films behave as disordered systems in the vicinity of a metal-insulator transition governed by defect density and by the arrangement of the building blocks.

2. GRM Characterization

To model the CT in GRM, we have chosen two easily processable GRMs to produce archetypal macroscopic thin films given by basal-plane-aligned network of partially oxidized graphene derivatives with tuned multiscale properties, such as degree of structural disorder, spatial distribution of defects, electrical resistivities, etc. In particular, a macroscopical physical observable as the electrical resistivity can vary by more than ten orders of magnitude according to defect density, oxygen content and structure.[6] We compare thin film based on single sheet reduced graphene oxide (RGO) and few-layer thick electrochemically exfoliated graphite nanoplateles (EGO). Using an approach previously demonstrated,[6a,7] we study CT comparing samples having similar macroscopic properties and tuning the mesoscopic ones. We benchmark devices with similar film thickness, semiconductive behavior and room temperature electrical resistivity, ρ_{RT}, but showing different spatial distribution of the defects and spatial disorder.

We study CT by combining microscopic and spectroscopic techniques to monitor the material properties from the nano- to macro- scale. To detect different CT regimes in these highly anisotropic thin films we analyzed systematically the resistivity, the magnetoresistance and the "noise" spectroscopy in the temperature range between 2 and 300 K. We also performed chemical, morphological and structural characterizations of the single nanosheet and thin films thereof, by using state-of-the-art methods such as X-ray Photoelectron Spectroscopy (XPS), Atomic Force Microscopy (AFM), Scanning Electron Microscopy

S. De Simone
Consiglio Nazionale delle Ricerche
Istituto per la Microelettronica e Microsistemi
(CNR-IMM) – Lecce Unit
SP Lecce-Monteroni km 1,200, Lecce 73100, Italy
C. Barone, S. Pagano
Dipartimento di Fisica "E.R. Caianiello"
Università degli Studi di Salerno
Via Giovanni Paolo II 132, Fisciano, SA 84084, Italy
C. Barone, S. Pagano
CNR-SPIN Salerno and INFN Gruppo Collegato di Salerno
c/o Università degli Studi di Salerno
Fisciano, SA 84084, Italy
M. Gobbi
CIC nanoGUNE
Tolosa Hiribidea 76, Donostia – San Sebastian E-20018, Spain
P. Samorì
Université de Strasbourg
CNRS
ISIS
8 allée Gaspard Monge, Strasbourg 67000, France
M. Affronte
Dipartimento di Scienze Fisiche
Informatiche e Matematiche (FIM)
via Giuseppe Campi 213/a, Modena 41125, Italy

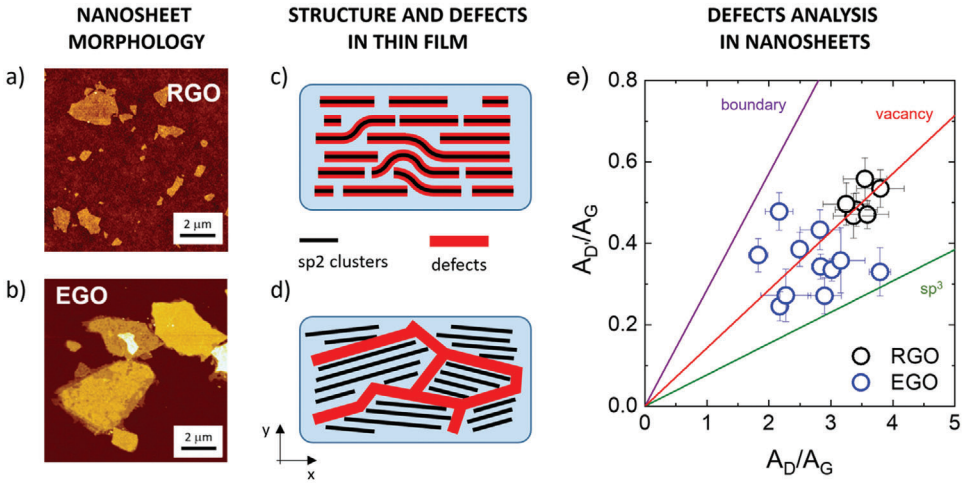

Figure 1. AFM images of a) RGO and b) EGO nanosheets; Z-range = 2.5 nm and 10 nm, respectively. c,d) Cross-sectional scheme of corresponding thin film packing and defect distribution at microscale. RGO thin films show a uniform distribution of defects overall all the graphenic planes while defects are arranged mainly at the external surface of EGO nanosheets. e) Characterization of defects by Raman spectroscopy on a representative statistical sample of 11 EGO and 6 RGO nanosheets. Variation in the relative intensity of the D′ band in terms of integrated area with the relative intensity of the D band for different graphene oxides. Solid lines correspond to the theoretical lines in the case of boundaries (purple), vacancies (red) and sp^3 defects (green), as calculated by Eckmann et al.[8]

(SEM), micro-Raman spectroscopy and X-Ray Diffraction (XRD) techniques.

3. Chemical and Morphological Structure of Single Nanosheets

3.1. Morphological Analysis of the Nanosheets

The two selected GRMs, i.e., RGO and EGO, displayed a different size and morphology, as evidenced by comparing surface root mean square roughness R_{RMS} (see Experimental Section) and thickness estimated by AFM analysis (**Figure 1**a,b); representative TEM images are reported in Figure S1 (Supporting Information). RGO is typically modeled as a purely monoatomic 2D sheet (nominal thickness = 0.6 ± 0.1 nm, as measured by AFM, see Figures S2a and S3c, Supporting Information) composed by a few nm sized sp^2 aromatic clusters separated by defective sp^2 areas and nanometric holes.[9] Such purely 2D nano-tessellation is confirmed by the R_{RMS} = 3 ± 1 Å measured on the single sheets, a value similar to that of the atomically flat silicon substrates. Differently, EGO displays an average thickness of 8 ± 2 nm given by a multi-layered structure (Figures S1, S2b, and S3f, Supporting Information). As described in details in ref.[10] oxygen atoms are not intercalated in-between layers of the multistack but they are rather mainly exposed on external surfaces, the latter exhibiting holes with diameters on the tens of nanometers scale and small adhered GO debris. The presence of such out-of-plane structures was already observed in functionalized graphene-like sheets[11] and yields a R_{RMS} value of the external surface of 5 ± 1 Å, exceeding the one measured on RGO. The lateral size of both nanomaterials is on the microscopic scale as they both display a broad and asymmetric distribution ranging between 100 nm and 3 μm. The average lateral size amounts to 300 ± 100 and 500 ± 200 nm for RGO and EGO, respectively. For more details see Experimental Section and Section S1 (Supporting Information).

3.2. Chemical Analysis and Defects of the Nanosheets

We combine a surface sensitive technique (XPS) and a bulk sensitive technique (Raman spectroscopy) to investigate the external layers of the nanosheets and the internal regions, respectively. The measured XPS spectra of the two GRMs (Figure S4, Supporting Information) show differences in the chemical composition, as reported in Table S3 (Supporting Information). RGO is composed in large majority by sp^2 carbon (93 ± 2%), sp^3 defects (ca 4%) with traces of oxygen (≤3%). Conversely, EGO is more complex, since it comprises a lower sp^2 aromatic content (ca 71%), a higher amount of sp^3 defects (ca 11%), and several oxidized functional groups such as epoxy (C–O–C), hydroxyl (C–OH), carbonyl (C=O) and carboxyl (O–C=O) groups. Considering the inelastic mean free path of C1s electrons,[12] we obtain that the first 2 nm contribute to 50% of the total signal of XPS (for more details see Experimental Section and Section S4, Supporting Information). The surface sensitivity of such technique highlights the different chemical nature of the outer surfaces of the two nanosheets and the corresponding different distribution of the defects. However, in the case of EGO the chemical composition of the layers is not uniform due to the many oxygen atoms and defects decorating the external surfaces leading to an overall underestimation of the aromatic component. The different dimensionality of the nanosheets corresponds to a different nanometric distribution of the defects in the thin film. Mainly localized on the surface of the nanosheets, defects distribute uniformly in RGO thin films while arrange forming sponge-like structures in the case of EGO (Figure 1c,d).

Density of defects and aromaticity in the entire nanomaterials, i.e., including their bulk, are investigated using Raman spectroscopy. The first-order Raman spectra of the two GRMs (Figure S5a, Supporting Information) can be deconvoluted into four bands: D, D", G and D'. Centered at 1587 cm^{-1}, G band corresponds to the contribution of the aromatic sp^2 regions, D

and D' are defect/disorder activated bands located at 1346 and 1618 cm^{-1} and D" at ≈1520 cm^{-1} is related to amorphous phases and wrinkled (defective) morphology of the sheets.[13] All the spectra of both GRMs show no shifts in peak positions with a maximum standard deviation of 4 cm^{-1}. In Figure 1e we correlate D and D' bands, expressed as the area of the peaks obtained by the deconvolution: $A_{D'}/A_G$ versus A_D/A_G. The measured values are compared to those obtained from ab-initio calculations (straight lines) used to simulate the Raman spectra of graphene with specific defects: boundaries, vacancies and sp^3 hybridization.[14] In the case of RGO, the measured values are all clustered around $A_{D'}/A_G \approx 0.5$ and $A_D/A_G \approx 3.5$, in excellent agreement with theoretical values, indicating that vacancies are the predominant defects. In contrast, datapoints of EGO nanosheets are more scattered, and indicate different relative contributions of boundary and vacancy and generic sp^3 defects.[8] In most of the cases, A_D/A_G ratios are larger for RGO indicating the presence of more defects with respect to EGO ($A_D/A_G = 2.7 \pm 0.4$), as confirmed by a lower $A_{2D}/A_{D+D'}$ and a wider D peak, as well. By using the relation proposed by Cançado et al.,[15] we assess the *in-plane* structure providing a rough estimate of the average size of aromatic sp^2 domains (L_{sp2}). The calculated values indicate an average aromatic size for EGO nanosheets = 7.5 ± 0.9 nm, that of RGO is slightly smaller = 5.6 ± 0.5 nm. Qualitative analysis of the second-order Raman bands (Figure S5b, Supporting Information) provides information of *out-of-plane* structure. In particular, 2D bands show different lineshape: i) symmetric for RGO in agreement with the purely bidimensional nature of the nanosheet and ii) multiple bands decomposed into several Lorentzian peaks in the case of EGO, confirming the multilayered structure.

Several works reported the correlation between the aromaticity and most of the Raman features. In addition to the area (A), the peak intensity (I) is a further parameter typically studied. Lopez et al.[16] showed that the ratio of the intensity of D and G peaks (I_D/I_G) roughly decreases linearly with increasing the sp^2 percentage. The measured I_D/I_G ratio values amount to 1.4 ± 0.1 and 1.2 ± 0.2 for RGO and EGO, respectively, clearly indicating that the sp2 content is > 80%. Moreover, we observed that such ratio decreases when the EGO thickness increases in agreement with the complex multilayer structure of the nanosheet, as discussed on XPS. In order to compare the aromaticity of the two GRM nanosheets we used a figure of merit combining the analysis of four parameters: G peak position and width, $A_{D+D'}/A_D$ ratio and D" peak position.[13,17] All such four features do not show remarkable difference between RGO and EGO (Table S4, Supporting Information) indicating that the sp^2 content of the two GRMs is quite similar.

4. Thin Films Electrical Measurements

We fabricate thin films of RGO and EGO having the same lateral dimensions (≈1 cm^2 area, ≈100 nm thick). Both types of films show similar bulk (3D) electric properties, with a negative temperature derivative of the resistivity near the disorder-induced metal-insulator transition (MIT) – typically indicating a semiconducting or glassy metallic behavior[18] – and room temperature resistivity (ρ_{RT}) amounting to $(2.0 \pm 0.2) \times 10^{-5}$ Ω·m and $(1.3 \pm 0.4) \times 10^{-4}$ Ω·m for RGO and EGO, respectively. Such values correspond to the averages calculated on a set of films with a thickness ranging within 20 to 220 nm (Figure S6a and Table S5, Supporting Information) and are halfway between ρ_{RT} of graphite in the direction parallel ($2.5\text{-}5.0\times10^{-6}$ Ω·m) and perpendicular (3×10^{-3} Ω·m) to the basal plane.[19]

To gain in-depth insight into the CT within the GRM thin films, we combined temperature-dependence of the electrical resistivity ρ(T), electrical noise and magnetoresistance (MR) measurements in the range between 2 and 300 K. **Figure 2**a shows the temperature-dependence of resistivity normalized to the value measured at room temperature (298 K): ρ/ρ_{RT} (black for RGO and blue for EGO). The absolute ρ(T) curves are reported in Figure S6b (Supporting Information). A dashed line shows an ideal power-law trend. We also report, as a reference standard, the ρ(T) curves of two different kinds of commercial, highly oriented pyrolytic graphite: HOPG-ZYH (red) and HOPG-ZYA (green). Figure 2b shows the ideal curve expected for bulk semiconductors, glassy metals and metals.

The energetic disorder of charge hopping sites is strongly correlated to the structural disorder of the material,[21] and is typically monitored by the empirical indicator *r*,[18d] defined as the ratio between the values measured at lowest (2 K) and room temperatures: $r = \rho_{2K}/\rho_{RT}$. Typically, *r* increases with the disorder of the material. Experimentally, we observe values of $r_{RGO} = 31$ and $r_{EGO} = 3.2$, thus indicating that the disorder degree measured in this way is correlated to the defect density observed by Raman, which showed a higher defect density for RGO as compared to EGO. The ρ(T) of both GRM thin films follows roughly a power-law curve, corresponding to a linear trend in log–log scale. EGO data show such behavior within the measured temperature range while RGO data diverge from linearity at low temperature (T < 20K). Both GRM thin films therefore behave as *disordered semiconductors* near the disorder-induced metal-insulator transition (MIT).[6a,22] The power-law curve corresponds to the *critical regime* where the resistivity (i.e., conductivity) neither follow metallic nor insulating behavior.[23] A detailed analysis of the involved dominant CT mechanisms is determined using the *reduced activation energy* (W), as proposed by Zabrodskii:[24]

$$W\ (T) = -\frac{d\ln\rho}{d\ln T} = -\frac{T}{\rho}\times\frac{d\rho}{dT} \quad (1)$$

The negative and positive trends of the W(T) plot correspond to the semiconducting and glassy (disordered) metallic regime, respectively. In the critical regime, W is constant, corresponding to a perfect power-law behavior of the resistivity with temperature. The transition to a metal ($d\rho/dT > 0$) corresponds to W = 0, i.e., the Mott–Ioffe–Regel limit.[25]

Figure 2c depicts the W(T) curve of RGO thin film in a log–log scale showing a negative trend corresponding to a semiconductive material near MIT. It points out three CT regimes at different temperatures: 1) T < 10 K shows a superlinear decay, 2) 10 K < T < 90 K shows a linear trend with negative slope = −1/2 (red line) corresponding to Efros-Shklovskii – Variable range hopping (ES-VRH),[26] and 3) T > 90 K shows a zero slope (green line) up to the room temperature corresponding to the critical regime described by a ρ(T) power-law (PL). Conversely, EGO thin film (Figure 4e) crosses the transition from semiconductive at T < 10 K (decreasing W trend) to a critical regime (10 K < T <

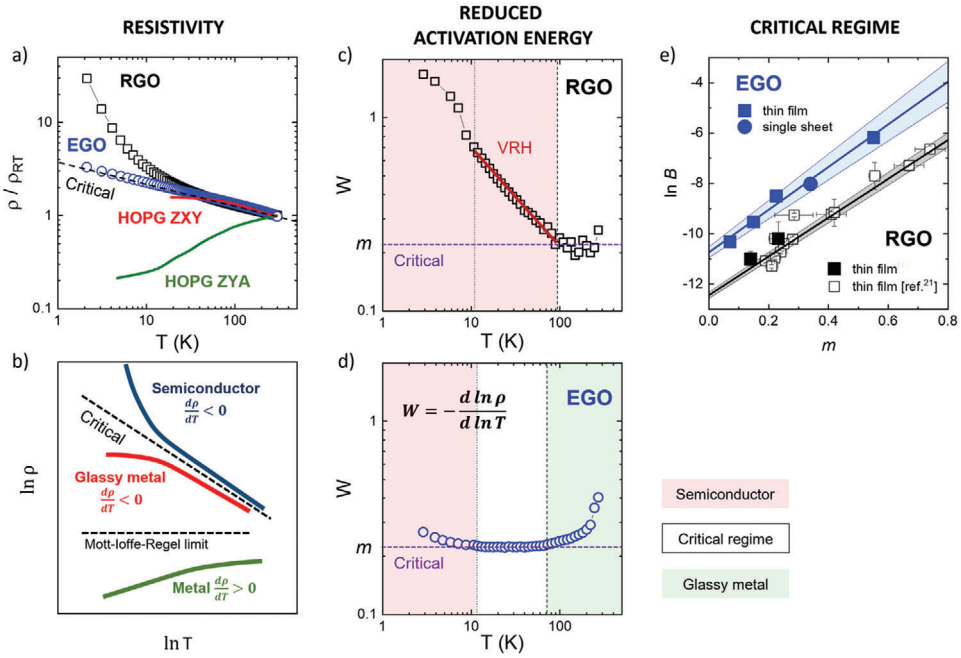

Figure 2. a) Temperature-dependence of resistivity on RGO (black) and EGO (blue) thin films. Log–log scale plots of ρ versus T normalized to the room temperature value (ρ/ρ_{300K}). Curve corresponding to HOPG ZHY and ZYA were digitalized from works,[20] respectively. b) Schematic plots of resistivity at the metal-insulator transition. c,d) Reduced activation energy W(T) measured in RGO and EGO thin films. e) PL regime analysis: ln B versus m obtained from W(T) for different devices: RGO and EGO thin film described in this work (filled squares), data from Kovtun et al.[6a] (open squares), single EGO flake (circle). The fitted linear trends (straight lines) are parallel, indicating that the RGO and EGO thin films follow the same CT mechanism with a given characteristic energy: $k_B T_{1,RGO} = k_B T_{1,EGO} = 190 \pm 40$ meV, being in excellent agreement with that previously reported in ref. [6a] calculated only considering the B standard error.

80 K), adopting a glassy metallic regime (increasing W trend) at T > 80 K. In the glassy metallic regime, the measured conductivity $\sigma = 1/\rho$ assumes the form $\sigma - \sigma_0 \sim T^{1/2}$ where $\sigma_0 \neq 0$ is the pure metallic conductivity (Figure S7, Supporting Information). Such temperature-dependence of the conductivity is due to electron–electron interaction effects in 3D disordered system.[25a] We previously demonstrated that in RGO thin film, VRH and PL regimes are strongly correlated, being both described by the localization length ξ calculated in the VRH regime.[6a] The thin film CT is governed by π-conjugated regions given by the overlapping aromatic clusters connected by a network of random paths with ξ as a characteristic length. In particular, ξ increases with the aromaticity and the film thickness as well, reaching an asymptotic behavior for $N_{layer} > 9$, corresponding to a bulk resistivity independent of the film thickness and therefore corresponding to a macroscopic 3D charge transport.

A similar approach cannot be directly extended to EGO due to the absence of the VRH regime. Thus, we focused on a detailed analysis of the critical regime (PL) observed in both GRM thin films. We shall use a model developed by Larkin and Khmelnitskii[23] to describe the CT of bulk (3D) disordered conductors near MIT from the dielectric side; in this model, the temperature-dependence of resistivity assumes the form: $\rho = (e^2 k_F/\hbar)\,(T/T_F)^{-m}$, where e is the electron charge, k_F is the Fermi wavevector, $\hbar$ the reduced Planck's constant, T_F is the Fermi temperature and $m < 1$. However, PL behavior is quite general and several physical models yield a similar functional dependence, e.g. Luttinger Liquid,[27] Coulomb blockade.[28] Moreover, Rodin[29] demonstrated that the PL behavior is not uncommon in the VRH regime of quasi-1D systems. Recently, Asadi et al.[30] demonstrated that the renormalized current-temperature characteristics of various polymers and devices at low voltage bias collapse on a PL curve developing an analytical description of CT based on polaron hopping mediated by nuclear tunneling. In order to rationalize such ubiquitous behavior, we can consider a general analytical form as $\rho = \rho_0\,(T/T_1)^{-m}$, with ρ_0 and T_1 corresponding to the characteristic resistivity and temperature, respectively. Such parameters are strongly coupled and the PL formula often reported in the literature is $\rho = BT^{-m}$, where B is the scale factor. Combining the two PL expressions, we obtain the general mathematical equivalence valid for each device:

$$\ln B = \ln \rho_0 + m \times \ln T_1 \quad (2)$$

Thus, we collected all the data in the correlation plot ln B versus m, (Figure 2e) corresponding to a set of 21 samples: ranging within a single nanosheet of EGO (blue circle) to RGO and EGO thin films, as measured (filled squares) and previously published (open black squares, see also Table S5, Supporting Information). All the data lay along two straight lines, one for each material. The linear dependence corresponds to a constant slope (ln T_1) and a Y-intercept (ln ρ_0), proving that a single of pair of characteristic parameters represents the CT behavior of each material: ($\rho_{0,RGO}$, $T_{1,RGO}$) and ($\rho_{0,EGO}$, $T_{1,EGO}$), respectively. As calculated by a linear fit according to Equation (2) we achieved the same slope for RGO and EGO thin films: ln $T_1 = 7.7 \pm 0.2$ and 8.0 ± 0.5, respectively,

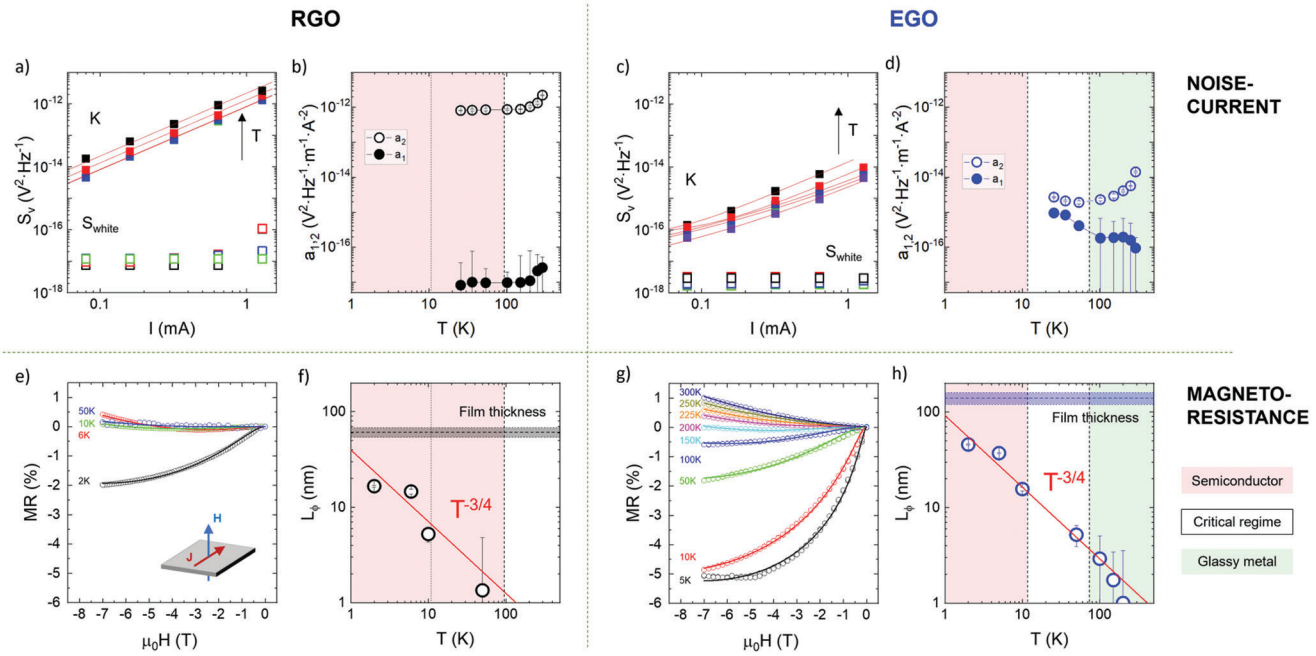

Figure 3. a–d) Noise-current measurements. Spectral density S_V of a) RGO and c) EGO films and b,d) the corresponding temperature dependence of the a_1 and a_2 parameters calculated using Equation (3). a,c) Filled and empty squares in violet, blue, red and black indicate values of K and corresponding S_{white} at increasing T. The red curves are the best-fit curves. The K value is estimated from S_V at 90 Hz, to avoid spurious peaks due to external sources, while the value of S_{white} is estimated from S_V above 10 kHz. e–h) Magnetic field dependence of the magnetoresistance MR of e) RGO and g) EGO thin films at different temperatures. For the sake of simplicity, we report only results obtained for negative *H*. The inset in (e) is a schematic illustration of the experimental transverse geometry where H and J denote the directions of the magnetic field and current flow, respectively. f,h) Temperature-dependence of L_ϕ calculated using Equation (4). Red lines are a guide for eyes. For sake of comparison, (f,h) show also the value of the film thickness, while a shadowed regions indicating the standard deviations of the thickness.

corresponding to a common characteristic energy $k_B T_1 = 190 \pm 40$ meV. A similar value has been recently measured on free-standing graphene oxide papers.[31]

5. Noise-Current Measurements

CT in disordered materials proceeds by a continuous release and trapping of charge carriers. The random behavior of such processes induces random fluctuations in the current flowing through the sample generating an electrical noise, which can be analyzed to provide further insight into the CT process. Thus, we investigated the CT mechanisms involved in the critical regime measuring the electrical noise in the temperature range from 20 K to room temperature (Figure S8, Supporting Information). In the case of graphene nanosheets the exact microscopic mechanism generating noise is still a matter of debate; it has been attributed to an effect due of the number charge carries and the mobility fluctuation model, or an interplay between the band-structure and sample inhomogeneity (see ref.[32] for more details). In general, noise current is mainly due to grain boundaries and edges.[33] Here we use a phenomenological approach to study GRM thin films correlating temperature- and current bias- dependencies. The measured noise-spectral density $S_V(f) = S_{white} + K/f^\gamma$ (**Figure 3**a,c) shows the presence of two uncorrelated components: the white noise (S_{white}) and the flicker one (K/f^γ), where typically $0.8 < \gamma < 1$. The first term is given by the sum of thermal, shot and background noise contributions,[34] resulting 2 orders of magnitude lower than the $1/f$ noise amplitude (K) at frequencies below 100 Hz on both GRM films. Generally, flicker noise exhibits a polynomial dependence with the bias current (i), the amplitude of which can be modeled as:

$$K(i,T) = a_2(T) \times i^2 + a_1(T) \times i + a_0 \quad (3)$$

where a_2, a_1 and a_0 are the quadratic, linear and constant phenomenological parameters, respectively. The quadratic term $a_2(T)$ is inversely proportional to the total number of mobile charge carriers in bulk metals and semiconductors,[35] the linear term $a_1(T)$ corresponds to a typical signature of the presence of non-equilibrium universal conductance fluctuations associated with weak-localization (WL) effects.[36] The constant term a_0 is due to the background readout electronics noise.[34a] The best-fit analysis of S_V is shown in Figure 3b,d. The quadratic term a_2 (open circles) is always significantly different from zero for both RGO and EGO thin films in the whole temperature range, implying that the leading mechanism producing current fluctuations is given by the mobility fluctuation, as observed in the graphene devices.[37] Moreover, the value measured in RGO is two orders of magnitude higher than in EGO, according to the larger defect density of RGO thin film. The a_1 parameter (filled circles) shows different behaviors in RGO and EGO. In RGO, a_1 is negligible in both the VRH and PL regimes confirming that the thin film behaves as a random resistor network, as identified in the resistivity analysis.[38] In EGO, instead, the presence of a linear component

observed in PL regime (i.e., both $a_1, a_2 \neq 0$) supports the presence of several contributions to charge transport mechanisms including the WL.

6. Magnetoresistance Measurements

The effect of WL on CT can be investigated by measuring the magnetoresistance ratio $MR(\%) = \frac{\rho_H - \rho_0}{\rho_0} \times 100\%$, defined as the relative change in resistivity due to applied magnetic field (ρ_H) with respect to the value measured in absence of magnetic field (ρ_0), at different temperatures ranging between 5 and 300 K (Figure 3e,g). A magnetic field H is applied along the out-of-plane directions (*transverse geometry*) observing symmetric results for positive or negative H. Both films show a temperature dependence of MR with negative values at low temperature and saturation at $H \approx -5$ T. RGO samples show $MR \neq 0$ for T < 10 K corresponding to the superlinear decay observed in W(T) analysis, and $MR \approx 0$ for all the other temperatures tested. Differently, EGO shows a smooth transition from negative MR at T < 100 K, to positive MR at T > 150 K, corresponding to the crossing from the critical regime and the glassy metal phase, as observed in metallic-like graphitic thin films,[39] and common metals.[40] The appearance of negative MR at low temperature in graphite materials is related to imperfections and lattice disorder.[41] Conversely, no negative MR is observed in perfect graphite crystals. Generally, magnetoresistance in the hopping transport regime is fitted by a standard expression,[5,42] determined by the sum of a linear ($\propto H$) and quadratic ($\propto H^2$) contribution arising from the quantum interference of different hopping paths and the contraction of charge-carrier wavefunction at impurity centers, respectively. However, it turns out that this model is not satisfactory to account for our data, as evidenced by the plots shown in Figure S9 (Supporting Information). Analogously, we ruled out a possible (bi)-polaronic mechanism since the expected low-field quadratic dependence is not observed. Thus, supported by the flicker noise analysis discussed above, we fit our MR data with the model predicted for 3D Weak Localization (3D-WL), as:[43]

$$MR = -\alpha\rho_0 \frac{e^2}{2\pi\hbar} \times \sqrt{\frac{eH}{\hbar}} \times F(x) + \beta H^2 \quad (4)$$

where α is a prefactor, e is the electronic charge, $\hbar$ is the reduced Plank's constant. $F(x)$ is the Hurwitz zeta function[44] with the dimensionless parameter $x = \frac{4eL_\phi^2}{\hbar}$, with L_ϕ the average distance a charge travels between inelastic collisions (i.e., phase coherence length). The last term βH^2 is usual quadratic magnetoresistance observed in bulk semiconductors.[45]

Both GRM thin film show similar behavior, the L_ϕ values calculated by Equation 4 (see Experimental Section) decrease with temperature increasing, as shown in Figure 3f,h, and systematically differ from zero at T < 100°K. The WL model reproduces RGO data only in the superlinear regime (at 50°K MR amounts ca 0.2%). Instead, it reproduces EGO data also in the critical regime of EGO; both findings agree with the flicker noise analysis. Moreover, the bulk (3D) behavior of MR is confirmed by several experimental findings: i) L_ϕ is lower than the film thickness throughout the measured temperature range; ii) L_ϕ is closely following the power $L_\phi \sim T^{-3/4}$ corresponding to electron–electron interaction with small energy transfer in 3D systems,[25a] and iii) L_ϕ is larger than the average aromatic size: $L_\phi > L_{sp2}$, as measured by Raman. The appearance of a metallic-like signature such as the WL in the magneto-transport and in the Flicker noise, despite a semiconductor like resistivity behavior, suggests that the charge carriers coherence extends on different planes thanks to the overlap of the 2D aromatic clusters allowing to circumvent the in-plane defects. Admittedly, the presence of alternative mechanisms leading to a similar $H + H^2$ dependence cannot be ruled out completely, since the quadratic term is temperature independent. Finally, we remark that the presence of localized magnetic moments due to vacancies and impurities could also lead to negative MR values. A detailed analysis would require the possibility to tilt the direction of the magnetic field parallel to the electrical current plane. Negative MR caused by scattering from localized magnetic moments originated from vacancies and impurities,[46] or the dominance of (bi-)polaronic mechanism,[47] can be excluded because the measured $MR \neq H^2$ (Figure S9, Supporting Information), as predicted by the corresponding models at low-field.

7. Structural Disorder

Considering that the inelastic scattering length is significantly larger than the estimated size of aromatic domains in RGO and EGO, the observed bulk CT coherent transport should be associated with charges traveling in multi-layered clusters. To better rationalize the CT, we thus analyzed the stacking and orientation of nanosheets in RGO and EGO sheets at the nanoscale, using XRD (see Figure S11, Supporting Information). We used specular scans to measure the vertical interplanar spacing of the stacked nanosheets (d, calculated by peak position using Bragg's law) and the average thickness of crystalline domain ($\boldsymbol{L}$ estimated using the Scherrer equation).[48] We then used rocking curves to study the crystal domains not perfectly parallel to the film surface (tilting angle $\varphi \neq 0$). In this case, the peak width corresponds to the mosaicity (or mosaic spread, $\boldsymbol{M}$) as the average mis-orientation of the crystalline domains with respect to the film plane: $\boldsymbol{M} = \langle\varphi\rangle$. In general, the greater the mis-orientation, the broader the peak of the rocking curve. Both specular scans (**Figure 4**a) show a main feature centered roughly in the region between 26.5° and 27° corresponding to the graphite (002) crystal plane along the out-of-plane direction (3.355 Å).[49] EGO shows a well-defined peak whose position gives an interlayer spacing of 3.37 Å. The domain size $\boldsymbol{L}$ amounts to 9 ± 1 nm showing a good agreement with the thickness of the EGO nanosheet amounting 8 ± 2, as discussed before. Differently, RGO exhibits a broader and less intense peak, indicating a more disordered packing; $\boldsymbol{L}$ amounts to 3–4 nm, corresponding to a domain given by 7–10 stacked nanosheets with ca 4 Å periodicity.

EGO rocking curve exhibits a narrower peak than RGO (Figure 4b) where the mosaic spreads amount 6.7 ± 0.1° and 12.8 ± 0.5°, respectively. Taking into account the thicker domains ($L_{z,EGO} > L_{z,RGO}$), such experimental evidence clearly indicate the higher order and orientation of EGO thin film structure. For the sake of comparison, the mosaic spreads of lower and higher quality pyrolytic graphite (i.e., HOPG ZYH

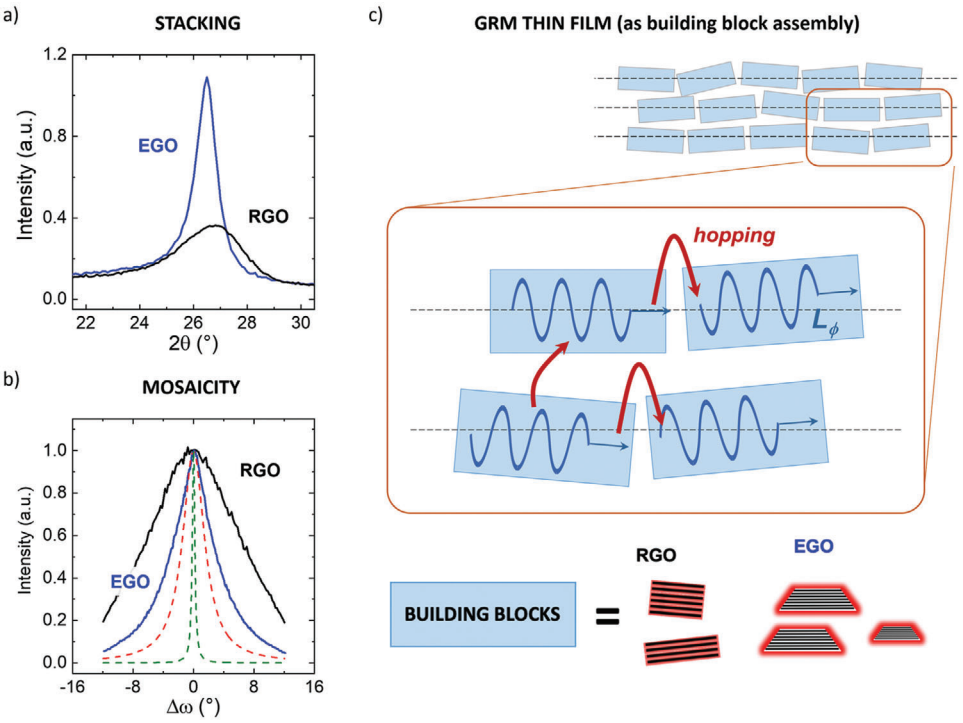

Figure 4. XRD data of RGO and EGO thin films. a) Specular scans and b) rocking curves. For the sake of comparison, rocking curves of HOPG ZYH (dot red line) and ZHA (dot green line) are shown. A scheme of the measurement conditions is depicted for each geometry. c) Scheme of thin films as assembly of poorly stacked building blocks. Different arrangements of the building blocks forming macroscopic assembly and their inner structure given by stacked layers. GRM thin films. The red and blue arrows denote coherent and incoherent charge transport paths, respectively.

and ZHA) amount 3.5 ± 1.5° and 0.4 ± 0.1°, respectively.[50] The main structural and chemical parameters of the two GRM thin films are summarized in **Table 1**. Further in-plane XRD measurements acquired at specular angle (Figure S12, Supporting Information) agrees with Raman results discussed above. While RGO shows a single symmetric peak corresponding to the in-plane carbon-carbon distance in the aromatic cluster, EGO show a complex peak line shape due to the presence of different defects distorting the carbon in-plane displacement.

Figure 4c provides a scheme of the film structure identified based on the abovementioned findings. GRM thin films are nano-aggregated materials given by networks of roughly parallel building blocks with similar lateral sizes but different internal structures and distribution of defects. In EGO, the building block corresponds to the single nanosheet, which can be described as a defective graphene 2D nanocrystal. Differently, in the case of RGO the building block is a stack of few nanosheets, with several defects on the outer sheets, and an inner, more graphitic core. Both of them are partially oxidized. Such scheme shows strong analogies with the semi-crystalline microstructures of conductive polymer thin films (see ref.[51] and references within) described as (more conductive) crystalline domains embedded within an (less conductive) amorphous matrix. The charge transport of the overall GRM thin film is given by the interplay of the mesoscopic 3D coherent transport inside the building block, as evinced by magnetoresistance analysis, and incoherent hopping among them showed by ρ(T) curves. Given the inhomogeneous disorder structure, how the charges travel through the overall thin film depends on the connection between the building blocks (percolation path) whose effective electrical connectivity requires a good face-to-face interaction corresponding to a relative parallel arrangement. Therefore, the percolative limit is approached as the mosaicity decreases. Such limit is also modulated by the thermal energy that leads to increase the hopping rate, i.e., thermally-induced metal-

Table 1. Chemical, structural and electric properties of GRM thin films studied by XPS, XRD and I-V measurements, respectively. (C sp^2) aromatic content, (O/C) oxygen to carbon ratio, (d) interlayer spacing, (L_z) crystalline domain average thickness, (M) mosaicity, (L_{sp2}) average aromatic size, (ρ_{RT}) room temperature electrical resistivity and resistivity ratio ($r = \rho_{2K}/\rho_{RT}$).

Thin film	C sp^2 [%]	O/C ratio	d [nm]	L_z [nm]	M [°]	L_{sp2} [nm]	ρ_{RT} [Ω×m]	$r = \rho_{2K}/\rho_{RT}$
RGO	93 ± 2	0.03 ± 0.01	0.334 ± 0.001	3.6 ± 0.1	10.7 ± 0.2	5.6 ± 0.5	(2.2 ± 0.2) × 10^{-5}	30
EGO	71 ± 2	0.15 ± 0.01	0.337 ± 0.001	8.8 ± 0.2	6.0 ± 0.1	7.5 ± 0.9	(11 ± 1)×10^{-5}	3.3

to-insulator transition. On the other hand, defects play a crucial role in the mesoscopic 3D transport governing the interlayer transport inside the building block, as recently reported by Çınar et al.[52]

8. Conclusion

In conclusion, we proposed a common framework to describe GRM thin films as bulk polycrystalline materials consisting in assemblies of mesoscopic quasi-2D domains. The CT in these regions can be described in analogy to CT in crystalline domains in semicrystalline conjugated polymers. GRM thin films behave as disordered systems in the vicinity of the metal-insulator transition (MIT) ranging between a semiconductor and a glassy metal, as governed by defect density and by the arrangement of the building blocks. Such general approach is supported by the findings of the detailed analysis of the sub-regimes. In particular, we unambiguously revealed that the critical regime of the two GRM thin films show the same "characteristic energy" strongly suggesting that the mechanism governing such regime is common to all GRM thin films. Previously indicated as polaron hopping mediated by nuclear tunneling, further investigations are underway to confirm the origin of such a mechanism and to shed light on the possibility that other processes (e.g., edge mobility) may occur. Since phase transition analysis describes the overall charge transport in thin films regardless of the mechanism at the nanoscale, the approach developed for GRMs can be also extended to describe the CT of disordered materials, such as vdW thin films, as well as composites and granular materials.

9. Experimental Section

Sample Preparation: GRM thin films were produced via wet chemistry: i) preparation of GRM suspension, ii) fabrication of GRM supported membrane and iii) its deposition on silicon oxide substrate.

GO was produced via modified Hummer's method.[53] Dried GO flakes were suspended in ultrapure deionized water at 2.5 mg mL^{-1} concentration. The obtained suspensions in water were sonicated mildly (Elma HP10 bath sonicator, frequency 37 KHz, Ultrasonic Power = 30 W) for 6 hours.

EGO was produced by electrochemical controlled oxidation and exfoliation of graphite using a two-step process: sodium perchlorate intercalation in acetonitrile and subsequent microwave treatment. The detailed procedure was reported in ref. [10] EGO was dispersed in *N*,*N*-Dimethylformamide (DMF) at 0.25 g L^{-1}.

GRM membranes were produced by means of vacuum-assisted filtration, using nylon 6,6 filter (pores: 0.2 µm; Axiva Sichem Pvt. Ltd.). Each membrane was produced using 0.4 mg of GRM in a mixture of ultrapure water/2-propanol (volume = 20 mL). Film thickness values amount 61 ± 7 nm for RGO and 140 ± 20 nm for EGO, respectively. GRM membranes were then mechanically transferred to Si (100) wafers coated by 300 nm SiO_2 layer thermally wet-grown (8 × 8mm^2; Siegert Wafer GmbH). The substrate was cleaned with plasma etching before the transfer procedure.

GO films transferred on substrate were thermally reduced at 900 °C in a tube furnace at high vacuum (pressure < 10^{-6} mbar) for 30 min. The annealing temperature was reached through a two-step process: a first ramp from room temperature up to 250 °C (rate = 1 K min^{-1}) and a subsequent fast one (rate = 5 K min^{-1}). No further treatment was instead performed on EGO films.

In order to avoid any direct electrical contact between the GRM films and Si (100) substrate, an area of material ≈1 mm width close to the substrate border was mechanically removed.

Charge Transport Measurements: Temperature-dependence resistivity ρ(T) and magneto-resistance (MR) measurements were carried out in 4-probes Van Der Pauw geometry.[54]

Cr/Au electrodes (5/50 nm thick) were thermally evaporated on the GRM thin films near the four edges in a square configuration (6 × 6 mm). Each electrode had a circular shape with 500 µm diameter.

In-plane, resistance measurements were performed in a PPMS cryostat (Quantum Design, USA) operating from room temperature down to liquid ^{4}He one (≈2 K). Biasing and measurement operations were made through an external Keithley 2636 SourceMeter connected by triaxial cables to the cryostat and controlled by a custom wrote LabView (NI Corp) code.

Electrodes on the film were micro-bonded to contact pads of the PPMS puck/sample holder. An ultrasonic bonder (mod. 4123, K&S Industries, USA) equipped with an aluminum wire was used.

All the measurements were performed by current biasing two electrodes and measuring the voltage drop at the other electrodes. The linearity of current–voltage characteristics was checked in the range of bias used, i.e., 10^2 nA (Figure S10, Supporting Information).

The electric noise characterizations were carried out in a dedicated experimental set-up, consisting in a closed-cycle refrigerator system (Janis Research) operating in the 8–325 K range with an active temperature stabilization of 0.2 K. The samples were biased, using a four probes contacts configuration, by a Keithley 220 Current Source. The output voltage signal was preamplified by specially designed low-noise electronics, having a background noise level of 1 nV/$\sqrt{Hz}$, and recorded by a dynamic signal analyzer HP35670A. All the readout circuitry was optimized for low-noise measurements,[55] and its effectiveness had been verified in several systems and devices.[56] The measurements were performed applying electrical field up to $\mathbf{E} \approx 200$ V m^{-1}, resulting 3 orders of magnitude higher than that applied in R(T) and magnetoresistance measurements ($\mathbf{E} \approx 0.2$ V m^{-1}). The effect of the electric field was taken into account by considering the effective temperature as a function of the field.[57] Details in Supporting Information "Chapter T_{eff}".

Magneto-resistance measurements were performed using a PPMS cryostat equipped with a superconducting magnet that can generate fields (μ_0H) up to 7T. The field was applied perpendicular to the basal plane of the GRM nanosheets network. Fitting procedure of MR curves. Equation 4 shows three fitting parameters: α, β and L_ϕ. β value is calculated by considering the curve MR ≠ 0 measured at the higher temperature: T = 10 K for RGO and 300 K for EGO, and subsequently fixed to this value in the fit of MR at lower temperatures.

Structural and Morphological Analysis: X-Ray Diffraction (XRD) measurements were performed by the Rigaku SmartLab diffractometer, equipped with a rotating copper anode (K_α: λ = 1.54184 Å). Two types of diffraction measurements were performed with a parallel beam: specular (or θ-2θ) scan and rocking curve. Specular scans were acquired between 2θ angles of 5° and 40°. Rocking curves were performed by fixing the detector at the Bragg peak position and rocking the incident angle.

X-ray Photoelectron Spectroscopy spectra (XPS) were acquired on GRMs films with a Phoibos 100 hemispherical energy analyzer (Specs GmbH) and Mg K_α radiation in constant analyzer energy mode. The overall spectrometer resolution was estimated to be equal to 0.9 eV (pass energy = 10 eV). Analysis chamber pressure during measurements was lower than 5 × 10^{-9} mbar. All XPS data were analyzed and processed with CasaXPS software (www.casaxps.com). The deconvolution procedure and the quantitative analysis of XPS C 1s survey were described in ref.[58] Inelastic mean free path corresponding to C1s photoelectrons was 2 nm.[12] XPS surface sensitivity is described in details in Supporting Information.

Atomic Force Microscopy (AFM) images were acquired with a scanning probe microscope (NT-MDT, Ntegra-I) in order to characterize GRM sheets, as well as GRM network surface and thickness. The instrument was operated in intermittent contact mode with a short n(Sb)-doped silicon cantilever (Brucker RTESPA-300, f = 300 kHz, k = 40

N/m). Image analysis was carried out with SPIP software (www.imagemet.com), details are reported in ref.[59] Size distribution of GRM sheets and Root Mean Square Surface Roughness (R_{RMS}) were measured by the analysis of a collection of AFM images corresponding to a total scan area of $\approx 10^5$ μm^2 and the analysis of 2473 RGO and 1719 EGO nanosheets. The surface coverage of nanosheets was ≈30%. Since the strong asymmetry of the size distributions the analysis was performed using percentiles: the average size D50 was defined as the median of the sample and the size range between D10 and D90, therefore, includes the most representative 80% fraction of the sample.[10] Thus, the size dispersion was described using the statistical parameters: median (D50) and median absolute deviation (MAD) instead of arithmetic mean and standard deviation (SD).[60] Details are described in Supporting Information.

Raman analysis had been performed by acquiring spectral maps with a Thermo Scientific DXR2xi Raman Imaging Microscope, equipped with a 50× objective and a 532 nm excitation laser. The maps were collected with a step-size of 0.5 μm, and each point spectrum resulted from 80 accumulations of 100 ms acquisitions. The reported spectra represent the average over single nanosheets.

Linear fitting analysis has been performed taking into account standard errors of all the experimental data using the York method.[61]

Supporting Information

Supporting Information is available from the Wiley Online Library or from the author.

Acknowledgements

The authors acknowledge the financial support of the Graphene Flagship Core 3 project (GA-881603). This work was partially supported by European Community through the FET-Proactive Project MoQuaS (GA-610449), the FLAGERA JTC 2017 MECHANIC, the ERC Advanced Grant SUPRA2DMAT (GA-833707), by the Italian Ministry for Research (MIUR) through the Futuro In Ricerca (FIR) grant RBFR13YKWX, by Chalmers University of Technology Foundation (Sweden) within the "Rune Bernhardsson's Graphene fund", and the Interdisciplinary Thematic Institute SysChem via the IdEx Unistra (ANR-10-IDEX-0002) within the program Investissement d'Avenir program, the International Center for Frontier Research in Chemistry and the Institut Universitaire de France (IUF). The authors are particularly grateful to Emanuele Treossi for providing GO, Rita Tonini for the scientific assistance with use the high-vacuum oven for the heat treatment, Francesco Maita and Gaetana Petrone for supporting measurements.

Conflict of Interest

The authors declare no conflict of interest.

Data Availability Statement

The data that support the findings of this study are available from the corresponding author upon reasonable request.

Keywords

charge transport, disordered systems, graphene, phase transition, Van der Waals thin films, weak localization

Received: April 17, 2023
Revised: June 5, 2023
Published online:

[1] A. Ciesielski, P. Samorì, *Chem. Soc. Rev.* **2014**, *43*, 381.
[2] a) Z. Lin, B. R. Carvalho, E. Kahn, R. Lv, R. Rao, H. Terrones, M. A. Pimenta, M. Terrones, *2D Mater.* **2016**, *3*, 022002; b) M. Tripathi, F. Lee, A. Michail, D. Anestopoulos, J. G. McHugh, S. P. Ogilvie, M. J. Large, A. A. Graf, P. J. Lynch, J. Parthenios, K. Papagelis, S. Roy, M. A. S. R. Saadi, M. M. Rahman, N. M. Pugno, A. A. K. King, P. M. Ajayan, A. B. Dalton, *ACS Nano* **2021**, *15*, 2520.
[3] a) Z. Lin, Y. Huang, X. Duan, *Nat. Electron.* **2019**, *2*, 378; b) K. S. Novoselov, A. Mishchenko, A. Carvalho, A. H. C. Neto, *Science* **2016**, *353*, aac9439.
[4] J. Rivnay, R. Noriega, R. J. Kline, A. Salleo, M. F. Toney, *Phys. Rev. B* **2011**, *84*, 045203.
[5] E. Piatti, A. Arbab, F. Galanti, T. Carey, L. Anzi, D. Spurling, A. Roy, A. Zhussupbekova, K. A. Patel, J. M. Kim, D. Daghero, R. Sordan, V. Nicolosi, R. S. Gonnelli, F. Torrisi, *Nat. Electron.* **2021**, *4*, 893.
[6] a) A. Kovtun, A. Candini, A. Vianelli, A. Boschi, S. Dell'Elce, M. Gobbi, K. H. Kim, S. L. Avila, P. Samorì, M. Affronte, A. Liscio, V. Palermo, *ACS Nano* **2021**, *15*, 2654; b) A. Vianelli, A. Candini, E. Treossi, V. Palermo, M. Affronte, *Carbon* **2015**, *89*, 188.
[7] M. N. Çınar, A. Antidormi, V.-H. Nguyen, A. Kovtun, S. Lara-Avila, A. Liscio, J.-C. Charlier, S. Roche, H. Sevinçli, *Nano Lett.* **2022**, *22*, 2202.
[8] A. Eckmann, A. Felten, A. Mishchenko, L. Britnell, R. Krupke, K. S. Novoselov, C. Casiraghi, *Nano Lett.* **2012**, *12*, 3925.
[9] a) K. Erickson, R. Erni, Z. Lee, N. Alem, W. Gannett, A. Zettl, *Adv. Mater.* **2010**, *22*, 4467; b) C. Gómez-Navarro, J. C. Meyer, R. S. Sundaram, A. Chuvilin, S. Kurasch, M. Burghard, K. Kern, U. Kaiser, *Nano Lett.* **2010**, *10*, 1144.
[10] Z. Xia, G. Maccaferri, C. Zanardi, M. Christian, L. Ortolani, V. Morandi, V. Bellani, A. Kovtun, S. Dell'Elce, A. Candini, A. Liscio, V. Palermo, *J. Phys. Chem. C* **2019**, *123*, 15122.
[11] J. P. Rourke, P. A. Pandey, J. J. Moore, M. Bates, I. A. Kinloch, R. J. Young, N. R. Wilson, *Angew. Chem., Int. Ed.* **2011**, *50*, 3173.
[12] H. Shinotsuka, S. Tanuma, C. J. Powell, D. R. Penn, *Surf. Interface Anal.* **2015**, *47*, 871.
[13] S. Claramunt, A. Varea, D. Lopez-Diaz, M. M. Velazquez, A. Cornet, A. Cirera, *J. Phys. Chem. C* **2015**, *119*, 10123.
[14] D. Lopez-Diaz, M. L. Holgado, J. L. Garcia-Fierro, M. M. Velazquez, *J. Phys. Chem. C* **2017**, *121*, 20489.
[15] L. G. Cançado, K. Takai, T. Enoki, M. Endo, Y. A. Kim, H. Mizusaki, A. Jorio, L. N. Coelho, R. Magalhães-Paniago, M. A. Pimenta, *Appl. Phys. Lett.* **2006**, *88*, 163106.
[16] D. López-Díaz, M. López Holgado, J. L. García-Fierro, M. M. Velázquez, *J. Phys. Chem. C* **2017**, *121*, 20489.
[17] B. Ma, R. D. Rodriguez, A. Ruban, S. Pavlov, E. Sheremet, *Phys. Chem. Chem. Phys.* **2019**, *21*, 10125.
[18] a) V. N. Prigodin, K. B. Efetov, *Phys. Rev. Lett.* **1993**, *70*, 2932; b) V. N. Prigodin, K. B. Efetov, *Synth. Met.* **1994**, *65*, 195; c) I. V. Gornyi, A. D. Mirlin, D. G. Polyakov, *Phys. Rev. Lett.* **2005**, *95*, 206603; d) M. N. Gueye, A. Carella, J. Faure-Vincent, R. Demadrille, J.-P. Simonato, *Prog. Mater. Sci.* **2020**, *108*, 100616.
[19] H. O. Pierson, *Handbook of carbon, graphite, diamond, and fullerenes : properties, processing, and applications*, Noyes Publications, Park Ridge, NJ, USA **1993**.
[20] a) G. Larkins, Y. Vlasov, K. Holland, *Supercond. Sci. Technol.* **2016**, *29*, 015015; b) D. B. Gutman, S. Tongay, H. K. Pal, D. L. Maslov, A. F. Hebard, *Phys. Rev. B* **2009**, *80*, 045418.
[21] M. Reghu, Y. Cao, D. Moses, A. J. Heeger, *Phys. Rev. B* **1993**, *47*, 1758.
[22] R. F. Milligan, T. F. Rosenbaum, R. N. Bhatt, G. A. Thomas, in *Modern Problems in Condensed Matter Sciences*, Vol. *10* (Eds: A. L. Efros, M. Pollak), Elsevier, New York **1985**.
[23] A. Larkin, D. Khmel'nitskii, *Sov. Phys. JETP* **1982**, *56*, 647.

[24] a) A. G. Zabrodskii, *Philos. Mag. B* **2001**, *81*, 1131; b) A. Zabrodsky, I. Shlimak, *Fizika Tekhn. Poluprov.* **1975**, *9*, 587.
[25] a) P. A. Lee, T. V. Ramakrishnan, *Rev. Mod. Phys.* **1985**, *57*, 287; b) J. H. Mooij, *Physica Status Solidi A Appl Res* **1973**, *17*, 521.
[26] B. I. Shklovskii, A. L. Afros, *Electronic Properties of Doped Semiconductors*, Springer, Berlin **1984**.
[27] M. Bockrath, D. H. Cobden, J. Lu, A. G. Rinzler, R. E. Smalley, L. Balents, P. L. McEuen, *Nature* **1999**, *397*, 598.
[28] A. J. Kronemeijer, E. H. Huisman, I. Katsouras, P. A. van Hal, T. C. T. Geuns, P. W. M. Blom, S. J. van der Molen, D. M. de Leeuw, *Phys. Rev. Lett.* **2010**, *105*, 156604.
[29] A. S. Rodin, M. M. Fogler, *Phys. Rev. Lett.* **2010**, *105*, 106801.
[30] K. Asadi, A. J. Kronemeijer, T. Cramer, L. Jan Anton Koster, P. W. M. Blom, D. M. de Leeuw, *Nat. Commun.* **2013**, *4*, 1710.
[31] K. Thamkrongart, H. Ramamoorthy, K. Buapan, T. Chiawchan, R. Somphonsane, *J. Phys. D: Appl. Phys.* **2022**, *55*, 245103.
[32] P. Karnatak, T. Paul, S. Islam, A. Ghosh, *Adv. Phys.: X* **2017**, *2*, 428.
[33] H. Lee, D. Cho, S. Shekhar, J. Kim, J. Park, B. H. Hong, S. Hong, *ACS Nano* **2016**, *10*, 10135.
[34] a) S. Kogan, in *Electronic noise and fluctuations in solids*, Cambridge Univ. Press, Cambridge **1996**; b) C. Barone, S. Pagano, *Coatings* **2021**, *96*, 96.
[35] F. N. Hooge, *Phys. Lett. A* **1969**, *29*, 139.
[36] a) C. Barone, F. Romeo, A. Galdi, P. Orgiani, L. Maritato, A. Guarino, A. Nigro, S. Pagano, *Phys. Rev. B* **2013**, *87*, 245113, b) C. Barone, F. Romeo, S. Pagano, C. Attanasio, G. Carapella, C. Cirillo, A. Galdi, G. Grimaldi, A. Guarino, A. Leo, A. Nigro, P. Sabatino, *Sci. Rep.* **2015**, *5*, 10705; c) M. Asa, C. Autieri, C. Barone, C. Mauro, S. Picozzi, S. Pagano, M. Cantoni, *Phys. Rev. B* **2019**, *100*, 174423.
[37] A. A. Balandin, *Nat. Nanotechnol.* **2013**, *8*, 549.
[38] a) P. Orgiani, A. Galdi, C. Sacco, R. Arpaia, S. Charpentier, F. Lombardi, C. Barone, S. Pagano, D. G. Schlom, L. Maritato, *J. Supercond. Novel Magn.* **2015**, *28*, 3481; b) A. Di Trolio, A. Amore Bonapasta, C. Barone, A. Leo, G. Carapella, S. Pagano, A. Polimeni, A. M. Testa, *Phys. Chem. Chem. Phys.* **2021**, *23*, 2368.
[39] Y. Ohashi, T. Hironaka, T. Kubo, K. Shiiki, *TANSO* **2000**, *2000*, 410.
[40] J. Ziman, *Principles of the Theory of Solids* Cambridge University Press, New York,**1964**.
[41] Y. Hishiyama, *Carbon* **1970**, *8*, 259.
[42] T.-I. Su, C.-R. Wang, S.-T. Lin, R. Rosenbaum, *Phys. Rev. B* **2002**, *66*, 054438.
[43] A. Kawabata, *Solid State Commun.* **1980**, *34*, 431.
[44] M. Abramowitz, I. A. Stegun, *Handbook of Mathematical Functions with Formulas, Graphs, and Mathematical Tables*, U.S. Govt. Print. Off, Washington **1964**.
[45] R. G. Mani, L. Ghenim, J. B. Choi, *Solid State Commun.* **1991**, *79*, 693.
[46] B. Muchharla, T. N. Narayanan, K. Balakrishnan, P. M. Ajayan, S. Talapatra, *2D Mater.* **2014**, *1*, 011008.
[47] P. A. Bobbert, T. D. Nguyen, F. W. A. van Oost, B. Koopmans, M. Wohlgenannt, *Phys. Rev. Lett.* **2007**, *99*, 216801.
[48] P. Puech, A. Dabrowska, N. Ratel-Ramond, G. L. Vignoles, M. Monthioux, *Carbon* **2019**, *147*, 602.
[49] W. H. Bragg, W. L. Bragg, *Proc. R. Soc. London, Ser. A* **1913**, *88*, 428.
[50] (Ed: Momentive).
[51] S. Fratini, M. Nikolka, A. Salleo, G. Schweicher, H. Sirringhaus, *Nat. Mater.* **2020**, *19*, 491.
[52] M. N. Çınar, A. Antidormi, V.-H. Nguyen, A. Kovtun, S. Lara-Avila, A. Liscio, J.-C. Charlier, S. Roche, H. Sevinçli, *Nano Lett.* **2022**, *22*, 2202.
[53] E. Treossi, M. Melucci, A. Liscio, M. Gazzano, P. Samorì, V. Palermo, *J. Am. Chem. Soc.* **2009**, *131*, 15576.
[54] L. J. van der Pauw, *Philips Res. Rep.* **1958**, *13*, 1.
[55] J. M. Routoure, S. Wu, C. Barone, L. Mechin, B. Guillet, *IEEE Trans. Instrum. Meas.* **2020**, *69*, 194.
[56] a) C. Barone, S. Pagano, I. Pallecchi, E. Bellingeri, M. Putti, C. Ferdeghini, *Phys. Rev. B* **2011**, *83*, 134523; b) G. Landi, C. Barone, C. Mauro, H. C. Neitzert, S. Pagano, *Sci. Rep.* **2016**, *6*, 29685; c) C. Barone, H. Rotzinger, J. N. Voss, C. Mauro, Y. Schön, A. V. Ustinov, S. Pagano, *Nanomaterials* **2020**, *524*, 524.
[57] H. Abdalla, K. van de Ruit, M. Kemerink, *Sci. Rep.* **2015**, *5*, 16870.
[58] A. Kovtun, D. Jones, S. Dell'Elce, E. Treossi, A. Liscio, V. Palermo, *Carbon* **2019**, *143*, 268.
[59] A. Liscio, *ChemPhysChem* **2013**, *14*, 1283.
[60] P. Bedson, T. J. D. Farrant, *Practical Statistics for the Analytical Scientist: A Bench Guide*, The Royal Society of Chemistry, London **2009**.
[61] D. York, N. M. Evensen, M. L. Martıńez, J. D. B. Delgado, *Am. J. Phys.* **2004**, *72*, 367.